Hosseini-Shokouh, Seyed Hossein; Zhou, Jin; Berger, Ethan; Lv, Zhong Peng; Hong, Xiaodan; Virtanen, Vesa; Kordas, Krisztian; Komsa, Hannu Pekka

Highly Selective H_2S Gas Sensor Based on $Ti_3C_2T_x$ MXene-Organic Composites

Published in:
ACS Applied Materials and Interfaces

DOI:
10.1021/acsami.2c19883

Published: 08/02/2023

Document Version
Publisher's PDF, also known as Version of record

Please cite the original version:
Hosseini-Shokouh, S. H., Zhou, J., Berger, E., Lv, Z. P., Hong, X., Virtanen, V., Kordas, K., & Komsa, H. P. (2023). Highly Selective H_2S Gas Sensor Based on $Ti_3C_2T_x$ MXene-Organic Composites. *ACS Applied Materials and Interfaces*, *15*(5), 7063-7073. https://doi.org/10.1021/acsami.2c19883

ACS APPLIED MATERIALS & INTERFACES

www.acsami.org

Research Article

Highly Selective H_2S Gas Sensor Based on $Ti_3C_2T_x$ MXene–Organic Composites

Seyed Hossein Hosseini-Shokouh, Jin Zhou, Ethan Berger, Zhong-Peng Lv,* Xiaodan Hong, Vesa Virtanen, Krisztian Kordas, and Hannu-Pekka Komsa*

Cite This: *ACS Appl. Mater. Interfaces* 2023, 15, 7063–7073

Read Online

ACCESS | Metrics & More | Article Recommendations | Supporting Information

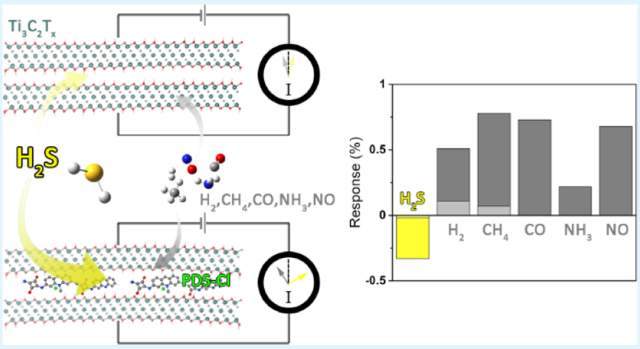

ABSTRACT: Cost-effective and high-performance H_2S sensors are required for human health and environmental monitoring. 2D transition-metal carbides and nitrides (MXenes) are appealing candidates for gas sensing due to good conductivity and abundant surface functional groups but have been studied primarily for detecting NH_3 and VOCs, with generally positive responses that are not highly selective to the target gases. Here, we report on a negative response of pristine $Ti_3C_2T_x$ thin films for H_2S gas sensing (in contrast to the other tested gases) and further optimization of the sensor performance using a composite of $Ti_3C_2T_x$ flakes and conjugated polymers (poly[3,6-diamino-10-methylacridinium chloride-*co*-3,6-diaminoacridine-squaraine], PDS-Cl) with polar charged nitrogen. The composite, preserving the high selectivity of pristine $Ti_3C_2T_x$, exhibits an H_2S sensing response of 2% at 5 ppm (a thirtyfold sensing enhancement) and a low limit of detection of 500 ppb. In addition, our density functional theory calculations indicate that the mixture of MXene surface functional groups needs to be taken into account to describe the sensing mechanism and the selectivity of the sensor in agreement with the experimental results. Thus, this report extends the application range of MXene-based composites to H_2S sensors and deepens the understanding of their gas sensing mechanisms.

KEYWORDS: *MXene, $Ti_3C_2T_x$, H_2S sensing, surface functional groups, density functional theory*

1. INTRODUCTION

Hydrogen sulfide (H_2S) is a toxic and flammable gas, largely found in petroleum and mining industries as well as in our daily life, e.g., putridity of foods and bacterial breakdown of human and animal wastes. Exposure to H_2S for humans has the risk of causing severe health problems such as eye and throat injury, dizziness, and loss of sense of reasoning at low concentrations, and it can even lead to death at a very high concentration (above 1000 ppm). According to the UK Health and Safety Executive standard, the short-term (about 8 h) exposure limit is 5 ppm.[1] Hence, the quality, performance, and accuracy of the detection sensors are very crucial. Most of the available H_2S gas sensors, however, are expensive and suffer from various problems such as high cost and power consumption, the high limit of detection (LOD), low selectivity, and inflexibility. Therefore, developing a readily available and low-cost gas sensor with better selectivity and LOD toward H_2S is necessary for human health and environmental monitoring.

Recently, two-dimensional (2D) materials (e.g., graphene,[2] MoS_2,[3] black phosphorus,[4] and MXene[5]) have attracted intensive research interest due to their unique physical and chemical properties, such as the large surface area, versatile surface chemistry, and room-temperature gas sensing capability.[6] Especially MXenes, consisting of 2D transition-metal carbides and nitrides, have shown promise for gas sensors due to outstanding metallic conductivity (10^3–10^4 S cm^{-1}), high mechanical stability, high hydrophilicity, and abundant surface chemistry for gas adsorption.[6] These layered materials have a universal formula of $M_{n+1}X_nT_x$, where M stands for early transition metals (Ti, V, Nb, Ta, Cr, Mo, etc.), X represents carbon and/or nitrogen, T_x denotes the hydrophilic surface functional groups, such as $=$O, $-$OH, or $-$F, and $n = 1$–3.[7,8] Lee et al. and Kim et al. were among the first to investigate gas sensing performance of pristine MXenes,[9,10] followed by a rapidly increasing number of studies.[11−15] In particular, the surface functional groups of MXenes provide a hydrophilic surface with highly negative zeta potentials, in the range of -30 to -80 mV, which facilitates efficient processing of hybrid

Received: November 4, 2022
Accepted: January 11, 2023
Published: January 25, 2023

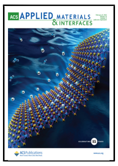

https://doi.org/10.1021/acsami.2c19883

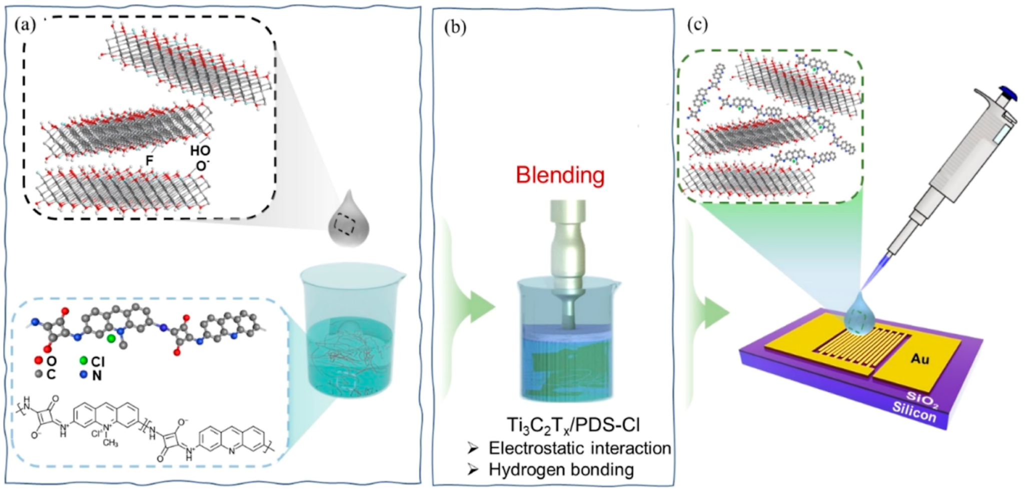

Figure 1. Schematic illustration of $Ti_3C_2T_x$/PDS-Cl composite synthesis and sensor fabrication: (a) after dissolving PDS-Cl polymer in water, the MXene ink was added to the polymer solution. (b) Tip sonication (for 2 min at 20 W) was utilized to facilitate the physical blending. (c) 1 μL of composite solution was drop-casted on prepatterned Au electrodes to fabricate the gas sensors.

MXene structures with organic polymers (with charged end-groups) in aqueous environment in contrast to other 2D materials. Forming composites of MXenes with organic materials has been already shown to be a feasible strategy to enhance both sensitivity and selectivity of gas sensors.[16−18] For instance, PEDOT:PSS/MXenes[6] and cationic polyacrylamide/MXene composites[19] showed a high response to NH_3, 36% at 100 ppm and 40% at 2000 ppm, respectively. However, despite the promising results, MXene-based gas sensors are still in their infancy and limited to sensors with a small response, constrained detection diversity with usually poor selectivity to the target gas. For example, to the best of our knowledge, only one H_2S gas sensor and one electrochemical H_2S sensor based on the $Ti_3C_2T_x$-related materials have been reported thus far[20,21] in which the sensing response for the gas sensor was mainly attributed to the Ag nanoparticles. Moreover, the intriguing role of intrinsic surface functional groups in the gas sensing performance has not been evaluated extensively even with theoretical calculations, which impairs the understanding of the sensing mechanism.

In this work, we investigate the gas-sensing performance of pristine $Ti_3C_2T_x$ and its nanocomposites with poly[3,6-diamino-10-methylacridinium chloride-*co*-3,6-diaminoacridine-squaraine] (PDS-Cl). While we observe clear H_2S selectivity (negative response) already on the pristine thin film of $Ti_3C_2T_x$ sensors, the composites of PDS-Cl polymer and $Ti_3C_2T_x$ ($Ti_3C_2T_x$/PDS-Cl) retain excellent selectivity toward H_2S and provide a higher surface to volume ratio for MXene flakes that consequently enhances the sensing response (∼30 times higher compared to pristine MXene at 1 ppm H_2S) with low detection limit (0.5 ppm) and good repeatability. To gain detailed insights into the interaction between gas molecules and $Ti_3C_2T_x$, we carried out density-functional theory (DFT) calculations, where we accounted for the fact that MXene surfaces contain a mixture of =O, −OH, and −F functional groups. We show that this has a dramatic effect on gas adsorption (charge transfer and adsorption energy) and is necessary for reproducing the experimental observations. Based on these, we finally propose a sensing mechanism.

2. EXPERIMENTAL SECTION/METHODS

2.1. Synthesis of $Ti_3C_2T_x$. Aqueous dispersion of $Ti_3C_2T_x$ was synthesized using the MILD method with minor modification.[22] In a typical synthesis, Ti_3AlC_2 (2 g, 325 mesh, Carbon-Ukraine) was added gradually to a stirring mixture of 40 mL 9 M HCl and 2 g LiF (2 g, 325 mesh, Sigma-Aldrich) at 35 °C. After 24 h, the product was separated by a centrifuge and washed with deionized water (DI) until pH > 5. 40 mL water was then added to the sediment and vortexed for 30 min. The supernatant containing few and multiple layered $Ti_3C_2T_x$ was obtained by centrifuging the mixture at 3500 rpm for 15 min and then storing at 4 °C before use. The concentration was measured by weighing a vacuum dried self-standing film of certain volume of the $Ti_3C_2T_x$ dispersion.

2.2. Synthesis of PDS-Cl. Acriflavine (230 mg, Sigma-Aldrich) and squaric acid (114 mg, Sigma-Aldrich) were dissolved in 15 mL pyridine and 35 mL *n*-butanol, respectively. The two solutions were mixed and then refluxed and stirred at 120 °C for 16 h under N_2 protection. After being cooled to room temperature, the mixture was filtered and washed using CH_2Cl_2, CH_3OH, and saturated NaCl aqueous solution. The obtained PDS-Cl was dried in an oven at 80 °C for 24 h. The product was collected as a dark brown powder.

2.3. $Ti_3C_2T_x$/PDS-Cl Composite Preparation. We synthesized poly[3,6-diamino-10-methylacridinium chloride-*co*-3,6-diaminoacridine-squaraine] (PDS-Cl), composited with $Ti_3C_2T_x$ through a facile in situ physical blending, as shown in Figure 1a,b. The weight percentage is calculated using eq 1

$$\text{wt}\ (\%) = \frac{w_{Ti_3C_2T_x}}{w_{\text{PDS-Cl}}} \times 100 \tag{1}$$

where $w_{Ti_3C_2T_x}$ and $w_{\text{PDS-Cl}}$ are the weights of the $Ti_3C_2T_x$ and PDS-Cl, respectively. Table S1 shows the required mass ratio of $Ti_3C_2T_x$ and PDS-Cl for samples with different wt % of $Ti_3C_2T_x$.

For instance, to prepare the $Ti_3C_2T_x$/PDS-Cl with a mass ratio of 4 wt %, 1 mg PDS-Cl was dispersed in 1 mL DI water by bath sonication for 30 min. After that, 3.3 μL of $Ti_3C_2T_x$ aqueous ink (C = 12 mg•mL^{-1}) was added to the solution followed by 2 min of tip sonication at 20 W to achieve uniform distribution of $Ti_3C_2T_x$. The same procedure was repeated for other mass ratios by changing the volume of $Ti_3C_2T_x$ aqueous ink.

2.4. Characterization. X-ray photoelectron spectroscopy (XPS) measurements were performed with a Thermo Fisher Scientific Escalab 250 XI system with an Al Kα source. Raman spectra were performed by a Thermo Scientific DXR2xi Raman imaging microscope (excitation wavelength, λ = 785 nm). The microstructure of synthesized material was studied by field-emission scanning electron

https://doi.org/10.1021/acsami.2c19883
ACS Appl. Mater. Interfaces 2023, 15, 7063−7073

microscopy (FESEM, Zeiss ULTRA plus and equipped with EDX), transmission electron microscopy (TEM, JEOL JEM-2200FS EFTEM/STEM 200 kV), and energy-dispersive X-ray elemental mapping. Fourier transform infrared spectroscopy (FTIR) of MXene−polymer hybrid was performed on a Spectrum Two FT-IR spectrometer with an ATR model (PerkinElmer, UK). The X-ray diffraction (XRD) was carried out by Rigaku Smart Lab 9 kW, Cu Kα-radiation with a 0.02° of step width. Dynamic light scattering (DLS) data were obtained using a Zeta sizer Nano ZS 90.

2.5. Sensor Fabrication and Gas Sensing Setup. To fabricate sensors, 1 μL DI dispersion (1 mg•mL^{-1}) of the $Ti_3C_2T_x$/PDS-Cl composite was drop-casted on the Si/SiO_2 substrate (4 × 6 × 0.5 mm), with 25 pairs of Au−Ti interdigitated electrodes (electrode distance and width were both 20 μm), to form a sensitive film and dried at room temperature, as shown in Figure 1c.

The sensing performance of materials was studied in a Linkam THMS600 heating and freezing stage connected to an Agilent 3458A multimeter at 1 V of constant bias, which are shown in Figure S1. Different concentrations of NH_3, NO, H_2S, CH_4, CO, and H_2 were obtained by LabView driven mass flow controllers. Nitrogen gas (N_2) and dry air were used as the carrier gas to dilute these gases to the desired concentrations, while the operating temperature was maintained at room temperature (30 °C). The total gas flow rate was kept constant at 100 mL min^{-1} in all experiments except for selectivity that it was 500 mL min^{-1}. To adjust the relative humidity level, an airflow was bubbled through a water-containing flask and then diluted with N_2 gas before introducing it into the test chamber. The ultimate humidity of the test gas was calibrated via a commercial humidity sensor.

2.6. Computational Methods. All DFT calculations were performed using cp2k software.[23−25] The PBEsol functional[25] was used with a Goedecker−Teter−Hutter (GTH)[26,27] pseudopotential and the Gaussian-type basis set MOLOPT.[28] Van der Waals interactions were accounted by adding the D3 dispersion correction.[29] A cutoff energy of 800 Ry was set for the expansion of the electron density in plane waves. Geometry optimizations were performed on 4 × 4 × 1 supercell using a 3 × 3 × 1 Monkhorst−Pack *k*-point grid. An out-of-plane lattice constant of 30 Å was used to provide a sufficiently large vacuum region (MXene thickness as calculated from the outermost H atoms is about 9.2 Å). The other lattice parameters were optimized for both mixed and fully O-terminated surfaces and the optimal values were then used and kept constant when adding the gas molecules. The charge transfer was computed using the Mulliken charges as directly implemented in cp2k. We defined it as the difference between the total MXene charge in the presence of and without the gas molecule. This means that a positive charge transfer represents electrons going from the molecule to the MXene layer. The adsorption energy E_a was defined as $E_a = E_{ads} - (E_{MXene} - E_{mol})$, where E_{ads}, E_{MXene}, and E_{mol} are the energies of the MXene layer with the adsorbed molecule, the pristine MXene layer, and the isolated gas molecule, respectively. The adsorption energy and charge transfer calculated without the D3 dispersion correction are listed in Table S2.

3. RESULTS

3.1. Material Characterization. We carried out material characterization for both pristine $Ti_3C_2T_x$ and its polymer nanocomposites. The polar charged structure of squaraine in PDS-Cl provides stronger electrostatic interactions between polymers and the $Ti_3C_2T_x$ flakes,[30] and it can offer ion−dipole interactions or hydrogen bonding with MXenes, forming numerous heterojunction interfaces that may benefit the gas-sensing properties of the composite. For instance, DLS data in Figure S2 show that increasing the MXene content gradually increases the average particle size from 371 nm in the pristine MXene to 4317 nm in PM-20. Such soft aggregation is caused by the electrostatic interaction between negatively charged MXene flakes and the positively charged quaternary ammonium cations in the PDS-Cl.[31]

Scanning electron microscopy (SEM) images of the composite, as shown in Figure 2a,b, show the heterojunction interfaces and the layered structures of $Ti_3C_2T_x$ flakes. This layered structure is also evident from the TEM analysis of pristine MXene, as shown in Figure 2c. TEM images of pristine $Ti_3C_2T_x$ and the composites (Figure 2c,d, respectively) indicate a successful blending of the MXene and polymer even for very thin samples, which is further supported by energy-dispersive X-ray (EDX) imaging that provides the elemental distribution of the composite structure, as shown in Figure S3. Pristine MXene sheets should be free of N and Cl but present in the polymer, whereas the opposite is true for Ti. Moreover, EDX indicates the presence of fluorine atoms that probably originate from the functional groups at the surface of the $Ti_3C_2T_x$ flakes.

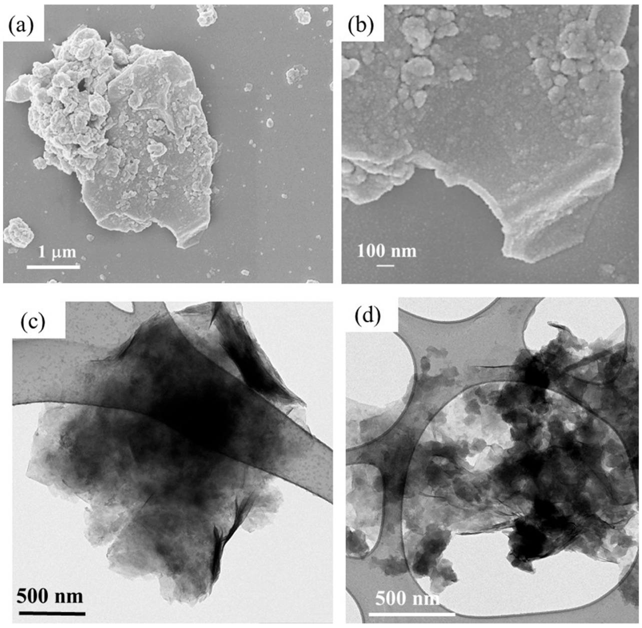

Figure 2. Microstructure analysis: (a) SEM and (b) high-resolution SEM images of samples with 10 wt % of MXene. TEM image of (c) pristine $Ti_3C_2T_x$ flakes and (d) composite sample with 10 wt % of the MXene.

Fourier transform infrared (FTIR) and Raman spectra of pristine $Ti_3C_2T_x$, PDS-Cl polymers, and the $Ti_3C_2T_x$/PDS-Cl composite, as shown in Figure 3, reveal the ionic nature of the PDS-Cl and the hydrogen bonding between the MXene flakes and the polymers. For a better comparison of FTIR and Raman spectra, we have only selected 3 composite samples (out of 6 samples utilized for gas sensing) with mass ratios of 4, 10, and 20 wt % denoted as MP-4, MP-10, and MP-20, respectively. In the FTIR spectrum for the PDS-Cl, as shown in Figure 3a, the peaks at 3322 and 3187 cm^{-1} are attributed to the N−H group. The feature at 1783 cm^{-1} can be attributed to the cyclobutene carbonyl compound (C═O),[32] which overlaps with expected C═N (imino) resonances at ca. 1780 cm^{-1}. The peak at 1544 cm^{-1} originates from the C═C stretching vibrations of four-membered ring while the characteristic strong absorption peak at 1610 cm^{-1} in PDS-Cl can be assigned to the vibration peak of the aromatic structure and zwitterionic resonance of the cyclobutene 1,3-diolate anion moiety, indicating the successful synthesis of the PDS-Cl with the anticipated structure, as shown in Figure 1a. The FTIR

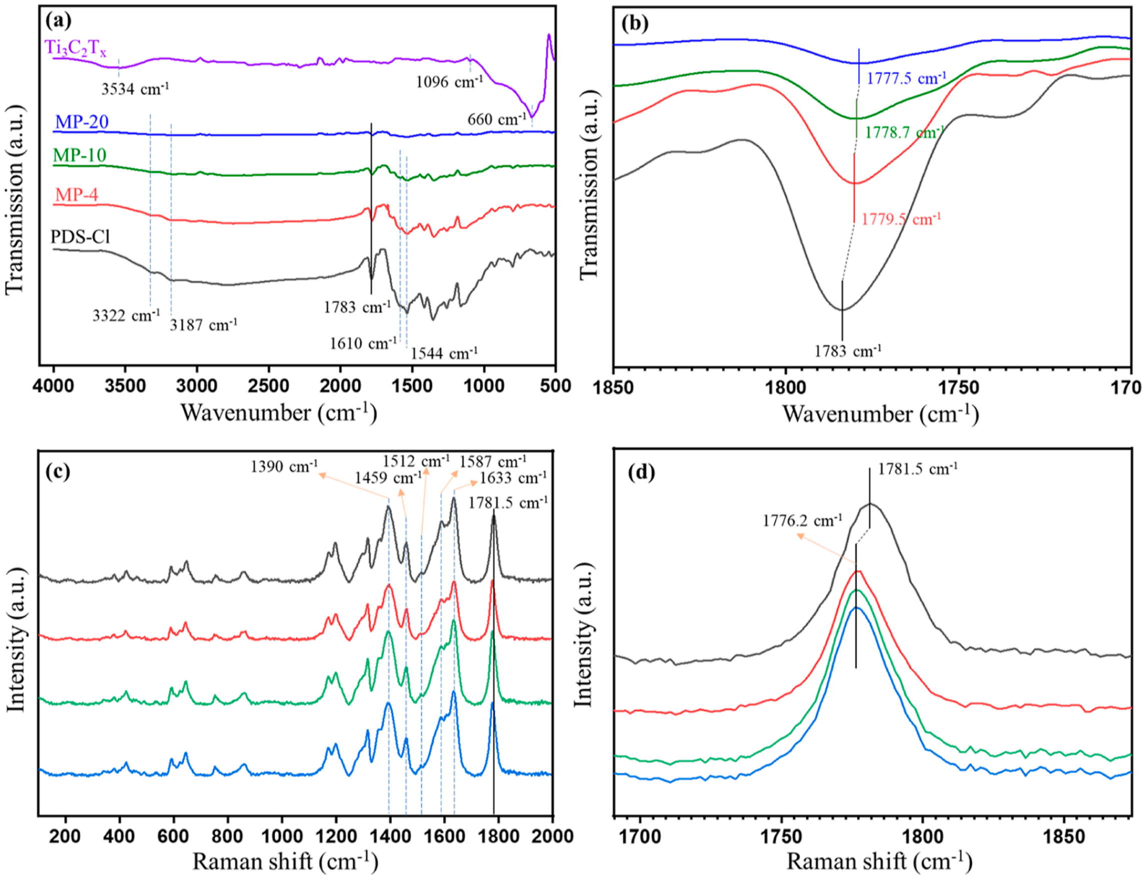

Figure 3. FTIR and Raman characterization: (a) FTIR spectra of pristine $Ti_3C_2T_x$, PDS-Cl, and composite samples (MP-4, MP-10, and MP-20) with color coding and labeled characteristic features. (b) Redshift of the C═O peak in the FTIR spectra. (c) Raman spectra of pristine $Ti_3C_2T_x$, PDS-Cl, and composite samples (MP-4, MP-10, and MP-20) along with (d) redshift of the C═O peak in Raman spectra.

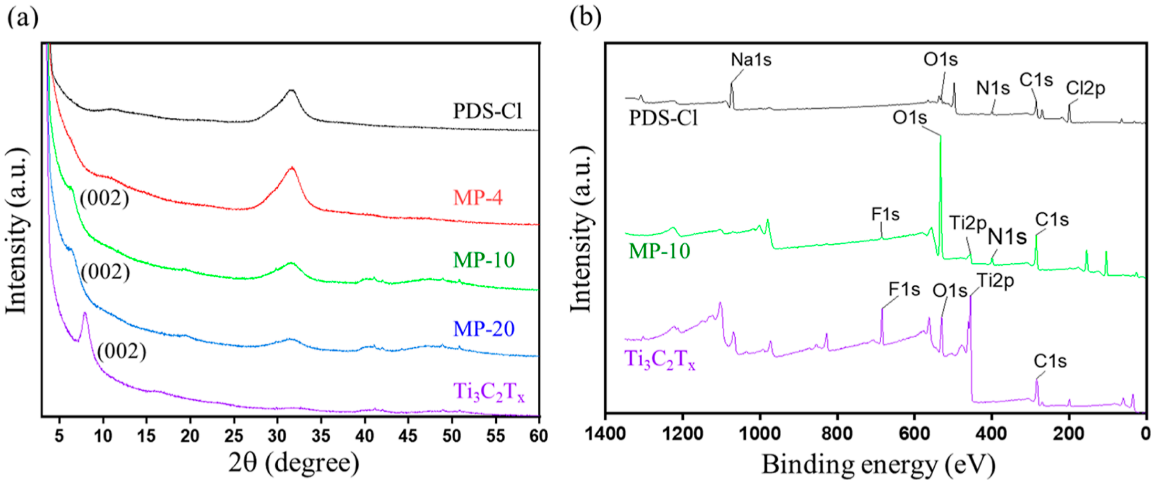

Figure 4. XRD and XPS analysis: (a) XRD spectra of pristine $Ti_3C_2T_x$, PDS-Cl, and composite samples. (b) Survey spectrum of $Ti_3C_2T_x$, PDS-Cl, and MP-10.

spectra of composites are almost similar to the PDS-Cl, except for the C═O stretching vibration (1783 cm^{-1}), which gradually redshifts from 1783.0 cm^{-1} in PDS-Cl to 1777.5 cm^{-1} in MP-20 (Figure 3b). This redshift probably originates from the electron density redistribution due to extra hydrogen bonding from the $Ti_3C_2T_x$ flakes.[33−35] For $Ti_3C_2T_x$, the peaks at 3534, 1096, and 668 cm^{-1} can be attributed to the stretching vibrations of −OH, C−F, and Ti−O bonds, in agreement with the previous reports.[36]

Raman spectra of PDS-Cl and composite samples also show a redshift (∼5 cm^{-1}) for the C═O peak at 1781.5 cm^{-1}, see Figure 3c,d. This spectrum also provides additional information about the PDS-Cl structure with the characteristic features attributed to the cyclic C═C stretching frequencies of cyclobutene (at 1633 cm^{-1}) and the quadrant and semicircle stretching vibrations of the aromatic ring at 1587 and 1512 cm^{-1}, respectively. Moreover, the vibration peaks of $N^+{-}CH_3$

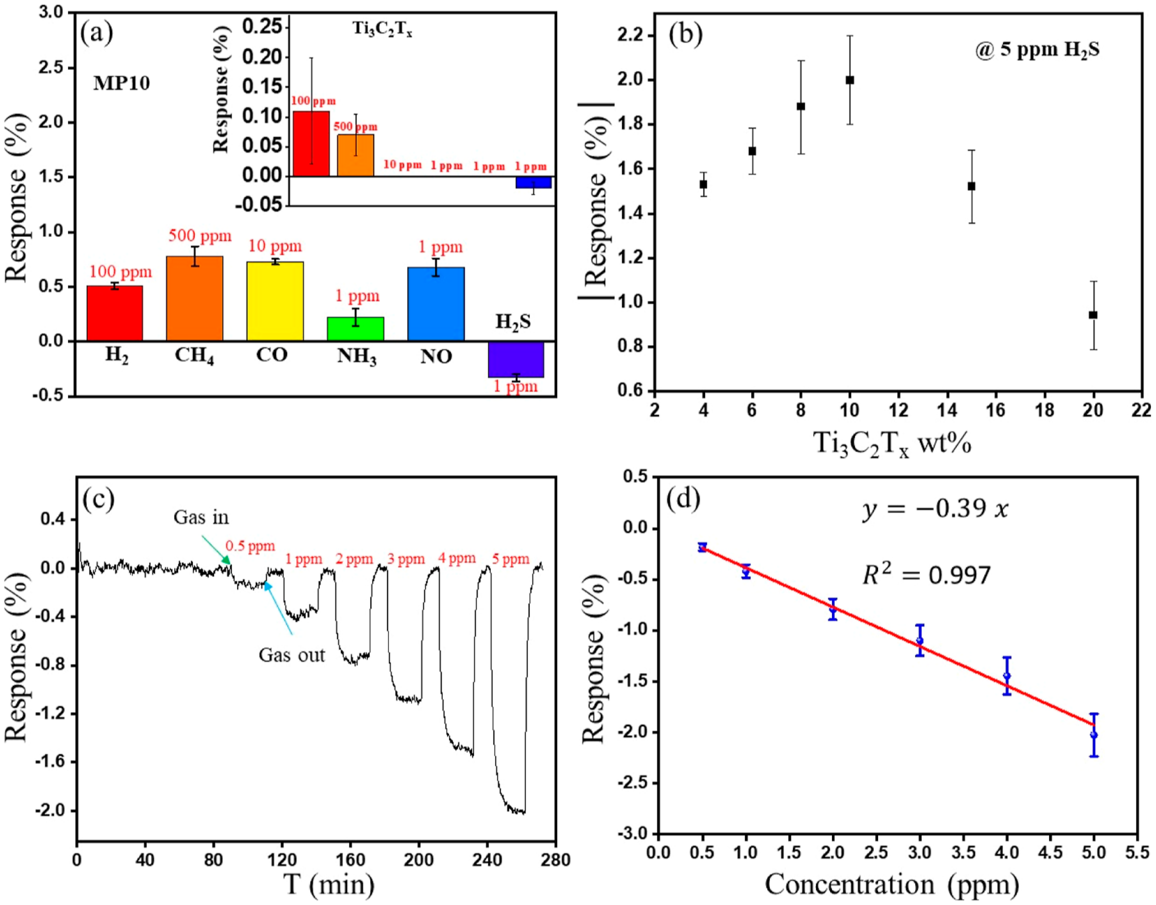

Figure 5. Selectivity and sensing response: (a) selectivity of MP-10 toward 6 different analytes with a negative response for H_2S. The inset shows the selectivity of pristine $Ti_3C_2T_x$. (b) H_2S sensing response for the composite samples with different mass ratios of $Ti_3C_2T_x$ in which the 10 percent shows the highest response. (c) Dynamic sensing response of MP-10 for different concentrations of H_2S, with the baseline subtracted for clarity and readability of the signal. (d) Sensing response of MP-10 sample versus H_2S concentration from 0.5 to 5 ppm (error bars indicate standard errors that are calculated using the data measured from three samples).

and C−N$^+$ (at 1459 and 1390 cm^{-1}, respectively) imply the ionic nature of PDS-Cl.[37,38]

Although the FTIR spectrum of pristine $Ti_3C_2T_x$ exhibits few characteristic features, as shown in Figure 3a, the Raman spectrum of thin films of $Ti_3C_2T_x$ and MP-10, dispersed on a Si substrate, indicates several features, as shown in Figure S4. Spectra show peaks at 123, 202, and 723 cm$^-$, which are assigned to the plasmonic resonance, the out-of-plane vibration of Ti, C, and surface group atoms, A_{1g} (Ti, C, and O), and the out-of-plane vibration of carbon atoms, A_{1g}(C), respectively. The intensity ratio of A_{1g}(C)/A_{1g} (Ti, C, O) varies depending on the sample.[39] For instance, this ratio for the pristine sample is around 0.86, which implies a strong A_{1g} (Ti, C, and O) vibration as whole flakes while for composites, it increases to 1.2 as a sign of weak coupling between flakes due to intercalation of polymers. Moreover, the A_{1g} (Ti, C, and O) peak for composite shifts to lower wavenumbers, ∼198 cm^{-1}, further indicating the disorder between the layers.[39]

XRD measurements also support the disorder between the $Ti_3C_2T_x$ flakes in the composites, as shown in Figure 4a. The characteristic reflection of the pristine $Ti_3C_2T_x$ at 8° (11.0 Å) shifts to 6.4° (13.8 Å) for MP-10 and MP-20 along with peak broadening and disappears for the MP-4 sample, implying increased interlayer separation and a disorder in the stacking of the $Ti_3C_2T_x$ flakes due to intercalation of PDS-Cl between layers.[40]

The functional groups, such as fluorine and oxygen, at the surface of the $Ti_3C_2T_x$ flakes and composite samples were evaluated using XPS. Figure 4b shows the survey spectrum of $Ti_3C_2T_x$, PDS-Cl, and MP-10, indicating the presence of those functional groups on the surface of the composite. The C 1s and F 1s spectra in Figure S5 indicate the interaction of carbon and fluorine in the MP-10 sample.[41] In the F 1s spectrum of the pristine MXene (Figure S5b), the peaks at 684.5 and 685.2 eV are assigned to F−Ti and C−Ti−F_x, respectively,[42,43] whereas the F 1s spectrum for MP-10 contains a third peak at 689.65 eV, suggesting the presence of the interaction between carbon and fluorine with high binding energy.

3.2. Gas Sensing Performance.

The gas sensors were fabricated by drop-casting equal amounts (1 μL of solution with concentration of 1 mg•mL^{-1}) but different mass ratios of the MXene/PDS-Cl composite onto SiO_2 (300 nm)-Si substrates. To find out the optimum mass ratio with the highest sensing response, we measured the H_2S response of composite samples with 6 different mass ratios of 4, 6, 8, 10, 15, and 20 wt %. Figure S6 shows the base resistance of the $Ti_3C_2T_x$/PDS-Cl composite samples, prior to gas sensing. A percolation threshold of $\varphi_0 = 6.00 \pm 1.10$ wt %, obtained by Belehradek power function fitting, indicates that all samples, other than 4%, contain conductive networks of MXene flakes.

The gas response is calculated using eq 2

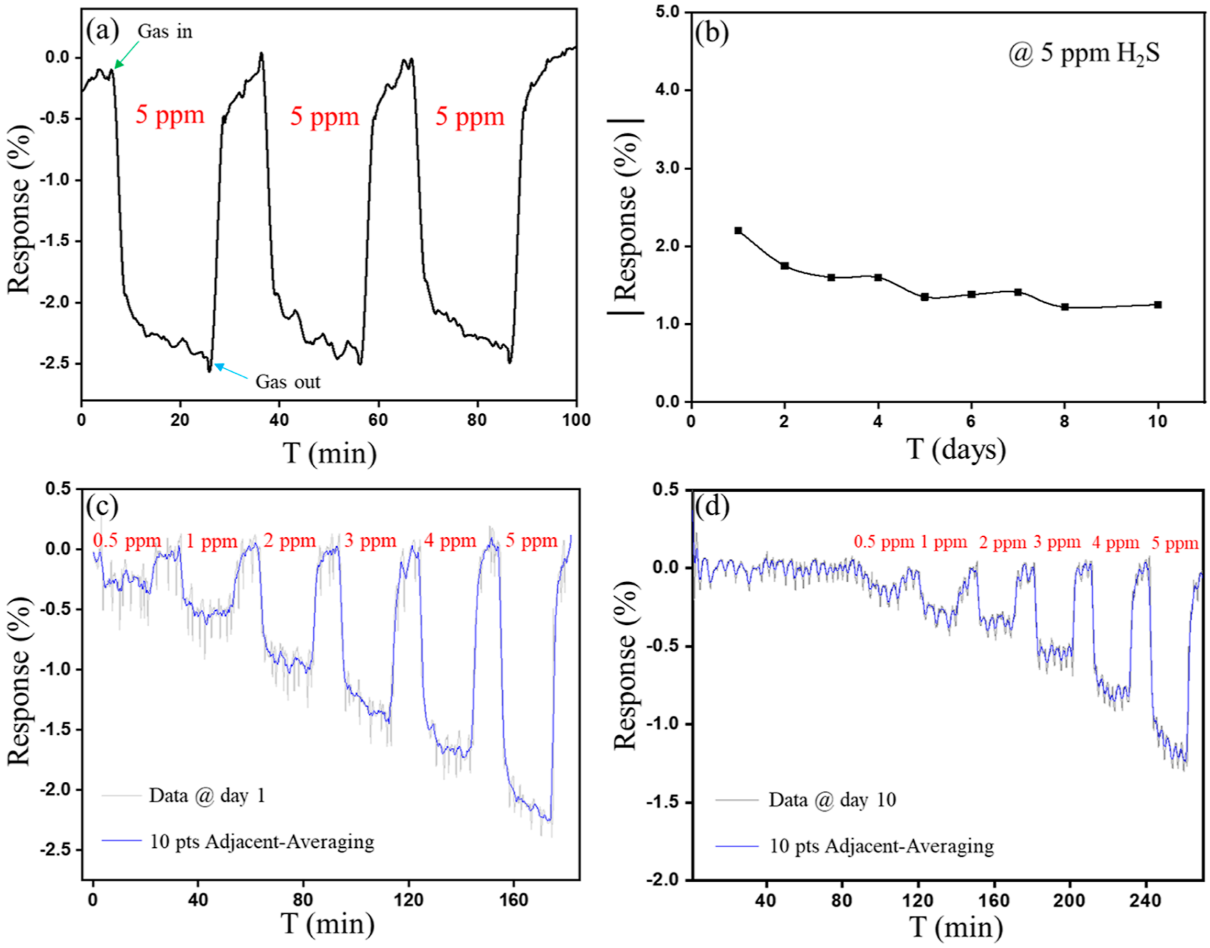

Figure 6. Repeatability and stability of sensor: (a) three cycles of MP-10 sensor response to 5 ppm H_2S at room temperature. (b) Stability of MP-10 sensor to 5 ppm H_2S over 10 days. The smoothed response−recovery curves of MP-10 sensor in day (c) 1 and (d) 10.

$$S\ (\%) = \frac{R_g - R_0}{R_0} \times 100 \tag{2}$$

where R_0 andR_g are the resistances of the sensor upon exposure to N_2 and the target gas, respectively.

Figure 5a summarizes the selectivity responses from the MP-10 sample, and the results from pristine MXenes, in the inset. The composite sensor shows striking selectivity toward the H_2S gas, with a negative response, while it is positive for all other analytes (see Figure S7 for real-time resistance curve of the sensor). Notably, the selectivity to H_2S is already present in the pristine MXene sensor, although the response is much smaller as shown in the inset of Figure 5a and Figure S8a.

Among all the samples, MP-10 shows the highest sensing response, around 2 ± 0.2% at 5 ppm of H_2S gas, as shown in Figure 5b, with a 30-fold increase of response at 1 ppm concentration of H_2S compared to the pristine $Ti_3C_2T_x$ (see Figure S8b). However, the noise level in MP-10 is higher compared to pristine $Ti_3C_2T_x$ in Figure S8b because the polymer alters the charge transport between layers. The real-time resistance curves of gas sensing for all samples (with different wt % of $Ti_3C_2T_x$) are shown in Figure S9.

Figure 5c shows the dynamic sensing response of the sensor for different concentrations of H_2S where the baseline is subtracted for clarity and readability of the signal. Despite the long pre-measurement exposure to N_2, around 1 h, the baseline is drifting; therefore, to calculate the correct response, a baseline curve, R_0 has been fitted and subtracted from the data. The sensor response is a linear function of the gas concentration with a low LOD as low as 0.5 ppm, see Figure 5d. To ensure the result for LOD, we took 40 data points at the baseline before the H_2S exposure in Figure 5c and calculated the noise level using the variation in the relative resistance change by the root-mean-square deviation.[44] The absolute value of the response for MP-10 (0.14%) is at least five times higher than the noise level (0.023%), confirming a LOD of 0.5 ppm. Finally, we note that the sensor response toward humidity was also positive, as shown in Figure S10, with enhanced responsivity, compared to pristine $Ti_3C_2T_x$.

The sensor shows very good repeatability with a small variation (standard deviation of 0.076) under consecutive exposure to the H_2S gas and recovers back to its initial state after gas removal, as demonstrated in Figure 6a.

The sensor stability under continuous measurements indicates that the response drops from −2.2 to −1.25% for 5 ppm of H_2S after 10 days, as shown in Figure 6b, indicating a 60% stability compared to the initial response. Figure 6c,d shows the sensor response to H_2S with concentrations varying from 0.5 to 5 ppm at day 1 and 10, respectively. The stability data is noisy, which could originate from the measurement setup rather than the material because exposure to the H_2S gas has no effect on the noise level. To improve the readability, the data have been smoothed with 10 points adjacent averaging method. Figure S11 demonstrates the real-time resistance curve of the sensor for H_2S sensing on days 1 and 10, in which the base resistance of the sensor increases in the course of time. Further studies are required to understand and enhance the stability, which might originate from the $Ti_3C_2T_x$ oxidation and can be suppressed by modifying the device preparation or structure.[13] In order to test the sensor's performance for real-world applications, we also measured the H_2S sensing performance of the MP-10 in an N_2/O_2 (80/20%) background, as shown in Figure S12, which indicates almost identical performance of the sensor.

3.3. H_2S Gas Sensing Mechanism. The pronounced H_2S selectivity may seem surprising in light of the previous results reported in the literature showing a positive response to all analytes. Pristine $Ti_3C_2T_x$ films were studied in refs 91045, and 48 and the general trends in the sensitivity agree with our results: sensitivity to ammonia and other "reactive" gases was high, but low to gases such as CH_4 and CO_2. In refs 10 and 45, all gases showed a positive response, but H_2S was not included in these studies. Wu et al. measured the H_2S response, but they only reported $|\Delta R|/R$, i.e., the sign of the response is unknown, and the gas concentration was very high (500 ppm).[45] Thus, although most papers have reported a positive response to any gas, the understanding of H_2S response is, in fact, limited.

Using in situ XRD, Koh et al. found that the positive response of "reactive" gases such as ethanol correlated with increasing interlayer separation of (Na-intercalated) Ti_3C_2.[46] This suggests a sensing mechanism, where the gases are intercalated between the layers and the resistivity increases due to the increasing interlayer separation of the conductive MXene sheets. Such a mechanism could explain the response to all gases with a positive response and the enhanced gas response in the MXene/polymer composite. However, the negative response (increasing conductivity) to H_2S requires an inherently different mechanism. Also, the linear I−V characteristics of MP-10 (Figure S13) suggest ohmic contact between the sensing film and the electrodes; therefore, the H_2S exposure modulates the conductivity of composites rather than contact resistance.

To gain insights into the possible sensing mechanism, we turned to atomistic modeling and DFT calculations. Because the negative response for H_2S was recorded already for pristine $Ti_3C_2T_x$ samples, we are looking for a mechanism that does not require the polymer but can still be enhanced by it. The majority of previously reported calculations have only considered pure O-terminated or pure OH-terminated surface.[10,45,47,48] However, it is known from NMR and neutron/X-ray scattering experiments that the surfaces contain a mixture of O, OH, and F groups,[49,50] and this functionalization is stable in vacuum or N_2 atmosphere.[51] In order to properly describe the interaction between the gas molecule and MXene surface, we thus adopt a model which contains a mixture of O, OH, and F groups in the $O_{0.50}OH_{0.25}F_{0.25}$ composition. The adopted model was found based on our previous investigation, reflecting typically reported compositions.[52] A significant concentration of O and F in our samples was also verified by EDX and XPS (Figures 2c and 4), although we cannot estimate the H concentration (i.e., the O/OH ratio) based on these methods. We note that gas adsorption on mixed-group surfaces of $Ti_3C_2T_x$ was studied by Khakbaz et al.,[53] but (i) these results were not compared to those from pure terminations and (ii) there was no detailed comparison to experimental results.

The charge transfers and adsorption energies of various gases on the pure O-terminated surface and the mixed-group surface are given in Table 1 and the adsorption geometries are depicted in Figure 7. The results are not only quantitatively but also qualitatively different owing to the larger variety of possible adsorption sites on the mixed surface and the different work functions (comparison of adsorption energies and charge transfer for similar sites are given in Table S2). We particularly note that H_2S and H_2O bind very strongly to mixed surfaces (much stronger than to the pure O-terminated surface) because the S atom of H_2S and O atom of H_2O can bind to the OH group and the H atoms to O groups. In fact, this result is fully consistent with reports of interlayer and surface water in MXenes (as observed, e.g., in TGA experiments),[54] arising from its high hydrophilicity.[55] NH_3 appears to have even stronger adsorption energy, although this situation is somewhat different. Because when NH_3 is adsorbed on the mixed surface, it captures a proton from one of the surface OH-groups (and 0.288e), resulting essentially in NH_4^+ adsorbed on negatively charged MXenes. We note that similarly high adsorption energies and NH_4^+ formation have been reported for mixed surfaces of vanadium carbide.[56] Such high adsorption energies would strongly favor analyte adsorption but rule out analyte desorption under ambient conditions, which is clearly not the case according to experiments. Instead, we propose that the omnipresent water will play a central role here in displacing the analytes from the surface, i.e., the analyte adsorption should rather be described by the adsorption energy difference with respect to H_2O.

Table 1. Charge Transfers and Adsorption Energies for the Different Molecules When Adsorbed on the Mixed Surface and the Purely O-Terminated Surface[a]

	mixed surface		purely O-terminated surface	
molecules	charge transfer	adsorption energy (meV)	charge transfer	adsorption energy (meV)
H_2	0.091	−270	0.069	−151
CH_4	−0.005	−216	0.008	−197
CO	0.152	−550	0.116	−248
NH_3	−0.288	−1349	0.316	−613
NO	−0.135	−448	0.321	−538
H_2S	0.163	−905	0.168	−383
H_2O	0.099	−1056	0.018	−263

[a] Positive values of the charge transfer represent electrons being transferred from the molecule to the surface. Only lowest energy configurations are shown, see Table S3 for the full version that includes results from other configurations.

The markedly higher work function of the O-terminated surface (calculated to be 6.17 eV[52] vs 4.3 eV for the mixed surface adopted here, Figure S15) is expected to lead to larger electron transfer from the analyte to MXene, i.e., more positive values for charge transfer in Table 1. This is indeed the case of CH_4 and NO on the O-site and H_2S on the O-site (Table S3). However, these are not the lowest energy configurations for NO and H_2S, and when the analyte is bonded to OH groups the charge transfer can be qualitatively different.

In light of the above discussion, two mechanisms are likely at play: (1) the intercalation-induced increase of the interlayer separation and (2) charge transfer-induced modifications in carrier density. Mechanism 1 will contribute to all analytes, but it will dominate whenever the adsorption energy of the analyte

https://doi.org/10.1021/acsami.2c19883
ACS Appl. Mater. Interfaces 2023, 15, 7063−7073

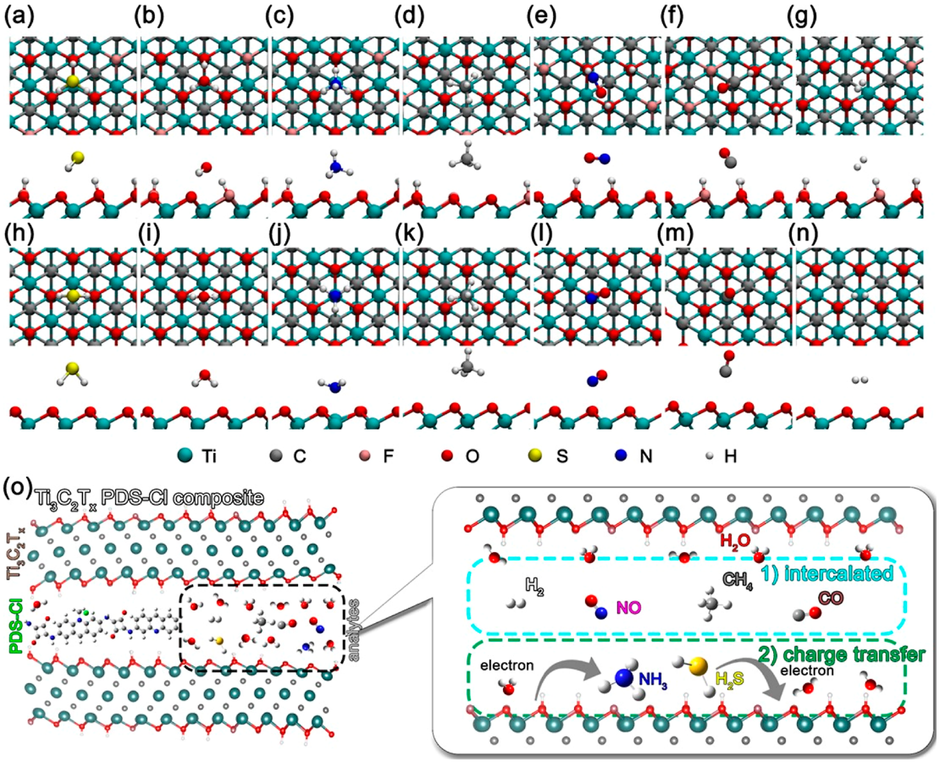

Figure 7. Adsorption geometries for different molecules on different MXene terminations: Panels (a–g) show the adsorption on a mixed surface ($O_{0.5}F_{0.25}OH_{0.25}$) for H_2S, H_2O, NH_3, CH_4, NO, CO, and H_2 molecules, respectively. Panels (d–n) show the adsorption on a pure O-terminated surface for the same respective molecules. Every panel has two parts: the top shows a top view of the MXene layer, while the bottom shows a side view of the MXene layer. Legend of the atom colors can be found at the very bottom of the figure. Panel (o) is the scheme of the proposed gas-sensing mechanism in which intercalation and charge transfer play the main role.

cannot compete with the H_2O adsorption and certainly includes H_2 and CH_4, perhaps also CO and NO. In all these cases, the response is positive irrespective of the direction of the calculated charge transfer. Mechanism 2 can dominate over mechanism 1 in the case of H_2S and NH_3 for which the adsorption energy is comparable or higher than that of H_2O. In order to estimate how the charge transfer would affect resistance, instead of ballistic conductance calculations,[57,58] we here rely on ref 59 where it was computationally shown that when O content of $Ti_3C_2T_x$ surfaces is more than 50%, an increasing electron concentration (positive charge transfer from the analyte) leads to increasing conductivity and thereby a negative sensor response,[59] as is the case with H_2S.

The response of NH_3 is more complicated, which makes it difficult to draw firm conclusions based on the calculations. Because NH_3 captures H^+ and 0.29e from MXenes, and H atoms in the OH group contains about 0.8e, 0.51e remains in the MXene and the response should be in the same direction as with H_2S, in contrast to the experiments. On the other hand, when abundant water is present, as discussed above, NH_3 can also capture protons from them, and then NH_4^+ adsorbed on the mixed surface is expected to accept ∼0.29e from the MXene. H^+ capture was not found in the calculations in ref 53 but found in ref 56 for vanadium carbide suggesting that it is sensitive to the surface composition. Furthermore, even though our films are thin, there are still multilayer MXene flakes as evidenced by XRD and the positive response from the intercalation might overcome the charge-transfer effect. After all, the adsorption energy of NH_3 (or NH_4^+) is very high and thus readily intercalated. The relatively slow recovery time of NH_3 (Figures S7 and S14) also points to a strong interaction.

In the case of MXene/PDS-Cl composites, the response is enhanced while the selectivity is preserved. As the polymer opens the interlayer spaces, the number of accessible active sites increases and the intercalation becomes easier. This can lead to enhancement of the charge-transfer effect (mechanism 2). As for mechanism 1, the situation is less clear: a larger concentration of intercalated analytes between the sheets can enhance the effect, while the induced changes in the interlayer separation might be reduced due to initially larger spacing. A final contribution arises from the geometrical effect, wherein the number of conductive paths is reduced with increasing polymer content (or decreasing the wt % of $Ti_3C_2T_x$; see resistance in Figures S5 and S8), which makes the sensor more sensitive (and noisy). On the other hand, the number of adsorption sites is expected to increase with increasing polymer content, and therefore there should be a trade-off for response as Figure 5b indicates. As the PDS-Cl/CNT composite also exhibits a small negative response toward H_2S whereas bare CNTs do not, see Figure S15. We cannot rule out a synergic effect based on the adsorption of analytes on the PDS-Cl. However, we note that the conductivity of bare PDS-Cl samples was below the detection limit of our instruments and according to our calculations, the MXene Fermi-level resides between the frontier orbitals of PDS-Cl (Figure S16) consistent with small conductivity.

4. CONCLUSIONS

In summary, we have observed high selectivity in pristine thin films of $Ti_3C_2T_x$ toward H_2S gas sensing. Utilizing conjugated PDS-Cl polymers, we could preserve the selectivity and enhance the gas-sensing response thirtyfold at 1 ppm. The optimized sensor with 10 wt % of MXenes indicated a response of 2% at 5 ppm with an LOD of 500 ppb. To shed light on the sensing mechanism, we carried out DFT calculations. We have accounted for the fact that MXene surfaces contain a mixture of O, OH, and F functional groups and show that this has a dramatic effect on the gas adsorption (charge transfer and adsorption energy). The experimentally observed trends could be reproduced relying on the analyte intercalation and the charge-transfer mechanism from adsorbed analytes in competition with water molecules. This report expands the MXene/organic heterojunction application and enhances the understanding of gas sensing mechanisms in MXene-based sensors.

ASSOCIATED CONTENT

Supporting Information

The Supporting Information is available free of charge at https://pubs.acs.org/doi/10.1021/acsami.2c19883.

> Required mass ratio of $Ti_3C_2T_x$ and PDS-CL for samples with different wt % of $Ti_3C_2T_x$; schematic of gas sensing setup; DLS data of pristine MXene, MP-4, 10, and 20; EDX imaging of the composite sample; Raman spectra of pristine $Ti_3C_2T_x$ and MP-10; XPS spectra for C 1s and F 1s; base resistance of composite sample with different weight ratios of $Ti_3C_2T_x$ along with power function fitting; real-time resistance curve of MP-10 sensor for different analytes; selectivity and real-time resistance curve of pristine $Ti_3C_2T_x$ for different concentrations of H_2S; I−V measurement of MP-10; real-time resistance curves; charge transfers and adsorption energies for the different molecules calculated with PBEsol functional but without van der Waals corrections; charge transfers and adsorption energies for the different molecules when adsorbed on the mixed surface and the purely O-terminated surface; and energy levels of the PDS-Cl polymer compared to the Fermi level of mixed MXenes (PDF)

AUTHOR INFORMATION

Corresponding Authors

Zhong-Peng Lv − *Department of Applied Physics, Aalto University, FIN-00076 Aalto, Finland;* orcid.org/0000-0002-0868-5126; Email: zhongpeng.lyu@aalto.fi

Hannu-Pekka Komsa − *Microelectronics Research Unit, Faculty of Information Technology and Electrical Engineering, University of Oulu, FIN-90014 Oulu, Finland;* orcid.org/0000-0002-0970-0957; Email: Hannu-Pekka.Komsa@oulu.fi

Authors

Seyed Hossein Hosseini-Shokouh − *Microelectronics Research Unit, Faculty of Information Technology and Electrical Engineering, University of Oulu, FIN-90014 Oulu, Finland;* orcid.org/0000-0002-2356-7611

Jin Zhou − *Microelectronics Research Unit, Faculty of Information Technology and Electrical Engineering, University of Oulu, FIN-90014 Oulu, Finland;* orcid.org/0000-0001-6433-2635

Ethan Berger − *Microelectronics Research Unit, Faculty of Information Technology and Electrical Engineering, University of Oulu, FIN-90014 Oulu, Finland;* orcid.org/0000-0001-9143-4493

Xiaodan Hong − *Department of Applied Physics, Aalto University, FIN-00076 Aalto, Finland;* orcid.org/0000-0003-0007-9356

Vesa Virtanen − *Research Unit of Medical Imaging, Physics and Technology, Faculty of Medicine, University of Oulu, 90220 Oulu, Finland;* orcid.org/0000-0002-5797-5365

Krisztian Kordas − *Microelectronics Research Unit, Faculty of Information Technology and Electrical Engineering, University of Oulu, FIN-90014 Oulu, Finland;* orcid.org/0000-0002-7331-1278

Complete contact information is available at: https://pubs.acs.org/10.1021/acsami.2c19883

Author Contributions

S.H.H.-S. and J.Z. contributed equally to this work. The experiments were designed and carried out by S.H.H.-S. and J.Z. (S.H.H.-S. conducted the XPS, TEM, SEM, electrical, and sensor measurements along with the data analysis; J.Z. synthesized the polymer and participated in electrical and sensor measurements along with the data analysis.) Z.-P.L. and X.H. synthesized the $Ti_3C_2T_x$ ink and provided the XRD, Raman DLS, and FTIR data. Raman measurement of the pristine MXene was performed by S.H.H.-S. and V.V. and DFT calculation and analysis were performed by E.B. and H.-P.K. Finally, S.H.H.-S. and J.Z. drafted the manuscript with the supervision of K.K. and H.-P.K. which was then discussed and revised by all authors.

Notes

The authors declare no competing financial interest.

ACKNOWLEDGMENTS

This work was financially supported in part by the University of Oulu (projects: Entity, ROAR, and Memristors and neuromorphic sensors from vertically aligned layered materials). We acknowledge funding from the EU Erasmus + programme (project: TACMEE), and the Academy of Finland (Center of Excellence Program in Life-inspired Hybrid Materials (LIBER), and projects: 311058, 325185, and 330214). We thank the personnel of the Centre for Material Analysis at the University of Oulu for providing us with technical assistance. We also thank CSC Finland for the generous grants of computer time.

REFERENCES

(1) Elwood, M. The Scientific Basis for Occupational Exposure Limits for Hydrogen Sulphide—A Critical Commentary. *Int. J. Environ. Res. Public Health* **2021**, *18*, 2866.

(2) Rao, C. N. R.; Gopalakrishnan, K.; Maitra, U. Comparative Study of Potential Applications of Graphene, MoS_2, and Other Two-Dimensional Materials in Energy Devices, Sensors, and Related Areas. *ACS Appl. Mater. Interfaces* **2015**, *7*, 7809−7832.

(3) Kim, Y.; Kang, S. K.; Oh, N. C.; Lee, H. D.; Lee, S. M.; Park, J.; Kim, H. Improved Sensitivity in Schottky Contacted Two-Dimensional MoS_2 Gas Sensor. *ACS Appl. Mater. Interfaces* **2019**, *11*, 38902−38909.

(4) Liu, Y.; Wang, Y.; Ikram, M.; Lv, H.; Chang, J.; Li, Z.; Ma, L.; Rehman, A. U.; Lu, G.; Chen, J.; Shi, K. Facile Synthesis of Highly Dispersed Co_3O_4 Nanoparticles on Expanded, Thin Black Phosphorus for a Ppb-Level NO_x Gas Sensor. *ACS Sens.* **2018**, *3*, 1576−1583.

(5) Kim, H.; Alshareef, H. N. MXetronics: MXene-Enabled Electronic and Photonic Devices. *ACS Mater. Lett.* **2020**, *2*, 55−70.

(6) Jin, L.; Wu, C.; Wei, K.; He, L.; Gao, H.; Zhang, H.; Zhang, K.; Asiri, A. M.; Alamry, K. A.; Yang, L.; Chu, X. Polymeric $Ti_3C_2T_X$ MXene Composites for Room Temperature Ammonia Sensing. *ACS Appl. Nano Mater.* **2020**, *3*, 12071−12079.

(7) Guo, J.; Legum, B.; Anasori, B.; Wang, K.; Lelyukh, P.; Gogotsi, Y.; Randall, C. A. Cold Sintered Ceramic Nanocomposites of 2D MXene and Zinc Oxide. *Adv. Mater.* **2018**, *30*, 1801846.

(8) Zhao, M. Q.; Xie, X.; Ren, C. E.; Makaryan, T.; Anasori, B.; Wang, G.; Gogotsi, Y. Hollow MXene Spheres and 3D Macroporous MXene Frameworks for Na-Ion Storage. *Adv. Mater.* **2017**, *29*, 1702410.

(9) Lee, E.; VahidMohammadi, A.; Prorok, B. C.; Yoon, Y. S.; Beidaghi, M.; Kim, D. J. Room Temperature Gas Sensing of Two-Dimensional Titanium Carbide (MXene). *ACS Appl. Mater. Interfaces* **2017**, *9*, 37184−37190.

(10) Kim, S. J.; Koh, H. J.; Ren, C. E.; Kwon, O.; Maleski, K.; Cho, S. Y.; Anasori, B.; Kim, C. K.; Choi, Y. K.; Kim, J.; Gogotsi, Y.; Jung, H. T. Metallic $Ti_3C_2T_x$ MXene Gas Sensors with Ultrahigh Signal-to-Noise Ratio. *ACS Nano* **2018**, *12*, 986−993.

(11) Xin, M.; Li, J.; Ma, Z.; Pan, L.; Shi, Y. MXenes and Their Applications in Wearable Sensors. *Front. Chem.* **2020**, *8*, 297.

(12) Deshmukh, K.; Kovářík, T.; Khadheer Pasha, S. K. State of the Art Recent Progress in Two Dimensional MXenes Based Gas Sensors and Biosensors: A Comprehensive Review. *Coord. Chem. Rev.* **2020**, *424*, 213514.

(13) Lee, E.; Kim, D.-J. Review— Recent Exploration of Two-Dimensional MXenes for Gas Sensing: From a Theoretical to an Experimental View. *J. Electrochem. Soc.* **2020**, *167*, 037515.

(14) Mehdi Aghaei, S.; Aasi, A.; Panchapakesan, B. Experimental and Theoretical Advances in MXene-Based Gas Sensors. *ACS Omega* **2021**, *6*, 2450−2461.

(15) Riazi, H.; Taghizadeh, G.; Soroush, M. MXene-Based Nanocomposite Sensors. *ACS Omega* **2021**, *6*, 11103−11112.

(16) Abu-Hani, A. F. S.; Awwad, F.; Greish, Y. E.; Ayesh, A. I.; Mahmoud, S. T. Design, Fabrication, and Characterization of Low-Power Gas Sensors Based on Organic-Inorganic Nano-Composite. *Org. Electron.* **2017**, *42*, 284−292.

(17) Ali, F. I. M.; Awwad, F.; Greish, Y. E.; Mahmoud, S. T. Hydrogen Sulfide (H_2S) Gas Sensor: A Review. *IEEE Sens. J.* **2019**, *19*, 2394−2407.

(18) Qiu, J.; Xia, X.; Hu, Z.; Zhou, S.; Wang, Y.; Wang, Y.; Zhang, R.; Li, J.; Zhou, Y. Molecular Ammonia Sensing of PEDOT:PSS/Nitrogen Doped MXene $Ti_3C_2T_X$ Composite Film at Room Temperature. *Nanotechnology* **2021**, *33*, 065501.

(19) Zhao, L. J.; Zheng, Y. Q.; Wang, K.; Lv, C.; Wei, W.; Wang, L. L.; Han, W.; Zhao, L. J.; Zheng, Y. Q.; Han, W.; Wang, K.; Lv, C.; Wang, L. L.; Wei, W. Highly Stable Cross-Linked Cationic Polyacrylamide/$Ti_3C_2T_x$ MXene Nanocomposites for Flexible Ammonia-Recognition Devices. *Adv. Mater. Technol.* **2020**, *5*, 2000248.

(20) Xu, Q.; Zong, B.; Li, Q.; Fang, X.; Mao, S.; Ostrikov, K. H_2S Sensing under Various Humidity Conditions with Ag Nanoparticle Functionalized $Ti_3C_2T_x$ MXene Field-Effect Transistors. *J. Hazard. Mater.* **2022**, *424*, 127492.

(21) Liu, X.; He, L.; Li, P.; Li, X.; Zhang, P. A. Direct Electrochemical H_2S Sensor Based on $Ti_3C_2T_x$ MXene. *ChemElectroChem* **2021**, *8*, 3658−3665.

(22) Alhabeb, M.; Maleski, K.; Anasori, B.; Lelyukh, P.; Clark, L.; Sin, S.; Gogotsi, Y. Guidelines for Synthesis and Processing of Two-Dimensional Titanium Carbide ($Ti_3C_2T_x$ MXene). *Chem. Mater.* **2017**, *29*, 7633−7644.

(23) Hutter, J.; Iannuzzi, M.; Schiffmann, F.; VandeVondele, J. Cp2k: Atomistic Simulations of Condensed Matter Systems. *Wiley Interdiscip. Rev.: Comput. Mol. Sci.* **2014**, *4*, 15−25.

(24) VandeVondele, J.; Krack, M.; Mohamed, F.; Parrinello, M.; Chassaing, T.; Hutter, J. Quickstep: Fast and Accurate Density Functional Calculations Using a Mixed Gaussian and Plane Waves Approach. *Comput. Phys. Commun.* **2005**, *167*, 103−128.

(25) VandeVondele, J.; Hutter, J. An Efficient Orbital Transformation Method for Electronic Structure Calculations. *J. Chem. Phys.* **2003**, *118*, 4365.

(26) Hartwigsen, C.; Goedecker, S.; Hutter, J. Relativistic Separable Dual-Space Gaussian Pseudopotentials from H to Rn. *Phys. Rev. B: Condens. Matter Mater. Phys.* **1998**, *58*, 3641.

(27) Goedecker, S.; Teter, M.; Hutter, J. Separable Dual-Space Gaussian Pseudopotentials. *Phys. Rev. B: Condens. Matter Mater. Phys.* **1996**, *54*, 1703.

(28) VandeVondele, J.; Hutter, J. Gaussian Basis Sets for Accurate Calculations on Molecular Systems in Gas and Condensed Phases. *J. Chem. Phys.* **2007**, *127*, 114105.

(29) Grimme, S.; Antony, J.; Ehrlich, S.; Krieg, H. A Consistent and Accurate Ab Initio Parametrization of Density Functional Dispersion Correction (DFT-D) for the 94 Elements H-Pu. *J. Chem. Phys.* **2010**, *132*, 154104.

(30) Boota, M.; Pasini, M.; Galeotti, F.; Porzio, W.; Zhao, M.; Halim, J.; Gogotsi, Y. Interaction of Polar and Nonpolar Poly Fl Uorenes with Layers of Two- Dimensional Titanium Carbide (MXene): Intercalation and Pseudocapacitance. *Chem. Mater.* **2017**, *29*, 2731−2738.

(31) Yan, J.; Ren, C. E.; Maleski, K.; Hatter, C. B.; Anasori, B.; Urbankowski, P.; Sarycheva, A.; Gogotsi, Y.; Yan, C. J. E.; Ren, K.; Maleski, C. B.; Hatter, B.; Anasori, P.; Urbankowski, A.; Sarycheva, Y.; Gogotsi, A. J.; Yan, J. Flexible MXene/Graphene Films for Ultrafast Supercapacitors with Outstanding Volumetric Capacitance. *Adv. Funct. Mater.* **2017**, *27*, 1701264.

(32) Larkin, P.*Infrared and Raman Spectroscopy, Principles and Spectral Interpretation*; Elsevier, 2011; pp 1−259.

(33) Nie, B.; Stutzman, J.; Xie, A. A Vibrational Spectral Maker for Probing the Hydrogen-Bonding Status of Protonated Asp and Glu Residues. *Biophys. J.* **2005**, *88*, 2833−2847.

(34) Joseph, J.; Jemmis, E. D. Red-, Blue-, or No-Shift in Hydrogen Bonds: A Unified Explanation. *J. Am. Chem. Soc.* **2007**, *129*, 4620−4632.

(35) Zhang, G.; Wang, W.; Chen, D. Chemical Origin of Red Shift of CO Stretching Vibration in Acetone Complexes with Various Metal Cations. *Chem. Phys.* **2009**, *359*, 40−44.

(36) Chen, J.; Yuan, X.; Lyu, F.; Zhong, Q.; Hu, H.; Pan, Q.; Zhang, Q. Integrating MXene Nanosheets with Cobalt-Tipped Carbon Nanotubes for an Efficient Oxygen Reduction Reaction. *J. Mater. Chem. A* **2019**, *7*, 1281−1286.

(37) Lin-Vien, D.; Colthup, N. B.; Fateley, W. G.; Grasselli, J. G.*The Handbook of Infrared and Raman Characteristic Frequencies of Organic Molecules*; Academic Press, 1991; pp 1−503.

(38) Colthup, N. B. Vibrating Molecular Models Frequency Shifts in Strained Ring Double Bonds. *J. Chem. Educ.* **1961**, *38*, 394−396.

(39) Sarycheva, A.; Gogotsi, Y. Raman Spectroscopy Analysis of the Structure and Surface Chemistry of $Ti_3C_2T_x$ MXene. *Chem. Mater.* **2020**, *32*, 3480−3488.

(40) Ling, Z.; Ren, C. E.; Zhao, M. Q.; Yang, J.; Giammarco, J. M.; Qiu, J.; Barsoum, M. W.; Gogotsi, Y. Flexible and Conductive MXene Films and Nanocomposites with High Capacitance. *Proc. Natl. Acad. Sci. U.S.A.* **2014**, *111*, 16676−16681.

(41) Reggente, M.; Angeloni, L.; Passeri, D.; Chevallier, P.; Turgeon, S.; Mantovani, D.; Rossi, M. Mechanical Characterization of Methanol Plasma Treated Fluorocarbon Ultrathin Films Through Atomic Force Microscopy. *Front. Mater.* **2020**, *6*, 338.

(42) Halim, J.; Cook, K. M.; Naguib, M.; Eklund, P.; Gogotsi, Y.; Rosen, J.; Barsoum, M. W. X-Ray Photoelectron Spectroscopy of Select Multi-Layered Transition Metal Carbides (MXenes). *Appl. Surf. Sci.* **2016**, *362*, 406−417.

(43) He, Y.; Wang, L.; Wang, X.; Shen, C.; Hu, Q.; Zhou, A.; Liu, X. Surface Reformation of 2D MXene by in Situ LaF_3-Decorated and Enhancement of Energy Storage in Lithium-Ion Batteries. *J. Mater. Sci.: Mater. Electron.* **2020**, *31*, 6735−6743.

(44) Li, J.; Lu, Y.; Ye, Q.; Cinke, M.; Han, J.; Meyyappan, M. Carbon Nanotube Sensors for Gas and Organic Vapor Detection. *Nano Lett.* **2003**, *3*, 929−933.

(45) Wu, M.; He, M.; Hu, Q.; Wu, Q.; Sun, G.; Xie, L.; Zhang, Z.; Zhu, Z.; Zhou, A. Ti_3C_2 MXene-Based Sensors with High Selectivity for NH_3 Detection at Room Temperature. *ACS Sens.* **2019**, *4*, 2763−2770.
(46) Koh, H. J.; Kim, S. J.; Maleski, K.; Cho, S. Y.; Kim, Y. J.; Ahn, C. W.; Gogotsi, Y.; Jung, H. T. Enhanced Selectivity of MXene Gas Sensors through Metal Ion Intercalation: In Situ X-Ray Diffraction Study. *ACS Sens.* **2019**, *4*, 1365−1372.
(47) Yu, X. F.; Li, Y. C.; Cheng, J. B.; Liu, Z. B.; Li, Q. Z.; Li, W. Z.; Yang, X.; Xiao, B. Monolayer Ti_2CO_2: A Promising Candidate for NH_3 Sensor or Capturer with High Sensitivity and Selectivity. *ACS Appl. Mater. Interfaces* **2015**, *7*, 13707−13713.
(48) Zhao, L.; Wang, K.; Wei, W.; Wang, L.; Han, W. High-performance Flexible Sensing Devices Based on Polyaniline/MXene Nanocomposites. *InfoMat* **2019**, *1*, 407−416.
(49) Shi, C.; Beidaghi, M.; Naguib, M.; Mashtalir, O.; Gogotsi, Y.; Billinge, S. J. L. Structure of Nanocrystalline Ti_3C_2 MXene Using Atomic Pair Distribution Function. *Phys. Rev. Lett.* **2013**, *112*, 125501.
(50) Wang, H. W.; Naguib, M.; Page, K.; Wesolowski, D. J.; Gogotsi, Y. Resolving the Structure of $Ti_3C_2T_x$ MXenes through Multilevel Structural Modeling of the Atomic Pair Distribution Function. *Chem. Mater.* **2016**, *28*, 349−359.
(51) Persson, I.; Näslund, L.-Å.; Halim, J.; Barsoum, M. W.; Darakchieva, V.; Palisaitis, J.; Rosen, J.; Persson, P. O. Å. On the Organization and Thermal Behavior of Functional Groups on Ti_3C_2 MXene Surfaces in Vacuum. *2D Mater.* **2017**, *5*, 015002.
(52) Ibragimova, R.; Puska, M. J.; Komsa, H. P. PH-Dependent Distribution of Functional Groups on Titanium-Based MXenes. *ACS Nano* **2019**, *13*, 9171−9181.
(53) Khakbaz, P.; Moshayedi, M.; Hajian, S.; Soleimani, M.; Narakathu, B. B.; Bazuin, B. J.; Pourfath, M.; Atashbar, M. Z. Titanium Carbide MXene as NH_3 Sensor: Realistic First-Principles Study. *J. Phys. Chem. C* **2019**, *123*, 29794−29803.
(54) Mashtalir, O.; Naguib, M.; Dyatkin, B.; Gogotsi, Y.; Barsoum, M. W. Kinetics of Aluminum Extraction from Ti_3AlC_2 in Hydrofluoric Acid. *Mater. Chem. Phys.* **2013**, *139*, 147−152.
(55) Zaman, W.; Matsumoto, R. A.; Thompson, M. W.; Liu, Y. H.; Bootwala, Y.; Dixit, M. B.; Nemsak, S.; Crumlin, E.; Hatzell, M. C.; Cummings, P. T.; Hatzell, K. B. In Situ Investigation of Water on MXene Interfaces. *Proc. Natl. Acad. Sci. U.S.A.* **2021**, *118*, No. e2108325118.
(56) Salami, N. First-Principles Realistic Prediction of Gas Adsorption on Two-Dimensional Vanadium Carbide (MXene). *Appl. Surf. Sci.* **2022**, *581*, 152105.
(57) Naqvi, S. R.; Shukla, V.; Jena, N. K.; Luo, W.; Ahuja, R. Exploring Two-Dimensional M_2NS_2 (M = Ti, V) MXenes Based Gas Sensors for Air Pollutants. *Appl. Mater. Today* **2020**, *19*, 100574.
(58) Pazniak, H.; Varezhnikov, A. S.; Kolosov, D. A.; Plugin, I. A.; Vito, A.; Glukhova, O. E.; Sheverdyaeva, P. M.; Spasova, M.; Kaikov, I.; Kolesnikov, E. A.; Moras, P.; Bainyashev, A. M.; Solomatin, M. A.; Kiselev, I.; Wiedwald, U.; Sysoev, V. V.; Pazniak, H.; Spasova, M.; Wiedwald, U.; Varezhnikov, A. S.; Plugin, I. A.; Bainyashev, A. M.; Solomatin, M. A.; Sysoev Yuri Gagarin, V. V.; Kolosov, D. A.; Glukhova, O. E.; Vito, A. D.; Sheverdyaeva, P. M.; Moras, P.; Kolesnikov, E. A. 2D Molybdenum Carbide MXenes for Enhanced Selective Detection of Humidity in Air. *Adv. Mater.* **2021**, *33*, 2104878.
(59) Bagheri, M.; Ibragimova, R.; Komsa, H. P. Fermiology of Two-Dimensional Titanium Carbide and Nitride MXenes. *Phys. Rev. B* **2021**, *104*, 035408.

https://doi.org/10.1021/acsami.2c19883
ACS Appl. Mater. Interfaces 2023, 15, 7063−7073